

# Wave–vortex decomposition of one-dimensional ship track data

By **OLIVER BÜHLER<sup>1†</sup>**,  
**JÖRN CALLIES<sup>2</sup>** AND **RAFFAELE FERRARI<sup>3</sup>**

<sup>1</sup>Courant Institute of Mathematical Sciences, New York University  
 New York, NY 10012, USA

<sup>2</sup>MIT/WHOI Joint Program in Oceanography, Cambridge/Woods Hole, MA 02139, USA

<sup>3</sup>Massachusetts Institute of Technology, Cambridge, MA 02139, USA

(Received 26 July 2014)

We present a simple two-step method by which one-dimensional spectra of horizontal velocity and buoyancy measured along a ship track can be decomposed into a wave component consisting of inertia–gravity waves and a vortex component consisting of a horizontal flow in geostrophic balance. The method requires certain assumptions for the data regarding stationarity, homogeneity, and horizontal isotropy. In the first step an exact Helmholtz decomposition of the horizontal velocity spectra into rotational and divergent components is performed and in the second step an energy equipartition property of hydrostatic inertia–gravity waves is exploited that allows diagnosing the wave energy spectrum solely from the observed horizontal velocities. The observed buoyancy spectrum can then be used to compute the residual vortex energy spectrum. Further wave–vortex decompositions of the observed fields are possible if additional information about the frequency content of the waves is available. We illustrate the method on two recent oceanic data sets from the North Pacific and the Gulf Stream. Notably, both steps in our new method might be of broader use in the theoretical and observational study of atmosphere and ocean fluid dynamics.

---

## 1. Introduction

The decomposition of a complex flow into various constituents that are distinguished by their intrinsic physical and mathematical properties is a powerful conceptual tool, which is particularly useful in the flows typical for the atmosphere and ocean, where small-scale dispersive waves, quasi-two-dimensional large-scale vortical flows along stratification surfaces, and pockets of three-dimensional turbulence all intermingle in a non-linear jigsaw puzzle. The most elementary of such flow decomposition methods is based on the linearized fluid equations relative to a state of rest, which for a rotating and stratified three-dimensional fluid system such as the Boussinesq model leads to the familiar decomposition into a horizontal flow in geostrophic and hydrostatic balance on the one hand and into unbalanced inertia–gravity waves on the other. However, even this most basic decomposition method in principle requires knowledge of all the flow variables throughout the entire three-dimensional domain, a task that is as straightforward in a numerical model as it is hopeless in observational practice.

† Author to whom correspondence should be addressed.

Indeed, many observations in the atmosphere and ocean are confined to a fixed location, or to a sequence of locations along a horizontal transect following an airplane flight or a ship track, say. In this latter situation it is possible to compute one-dimensional spectra along the ship track of flow variables such as the horizontal velocities or the buoyancy. By assuming stationarity and homogeneity as needed, this allows the estimation of one-dimensional covariance functions or, equivalently, of one-dimensional power spectra. Of course, such ship track data is highly aliased in the sense that the power spectra at the one-dimensional wavenumber  $k > 0$  along the ship track, say, are affected by the multi-dimensional dynamics associated with all wavenumber vectors with magnitude greater or equal to  $k$ . The situation improves if one can assume horizontal isotropy at least, in which case one can exploit the link between one-dimensional and isotropic two-dimensional spectra. In particular, one can then exploit the well-known differences between the power spectra of along-track and across-track velocity components (e.g. Batchelor 1953; Charney 1971) to gain some insight into the dynamics of the underlying flow, such as its decomposition into waves and other constituents.

These issues are of pressing concern especially in oceanography, where observations are sparse and our understanding of the relevant dynamical processes is poor. For example, the oceanic motions are very energetic in the submesoscale horizontal range between  $O(100)$  km, the scale of the Rossby radius of deformation, and  $O(1)$  km, the smallest scale at which rotation strongly affects dynamics. These motions play an important role in the overall ocean circulation, because they connect the large scales where the ocean is energized by atmospheric forcing to the small scales at which energy is dissipated (Ferrari & Wunsch 2010). Despite the explosion of theoretical studies of submesoscale dynamics in the last decade, the dearth of observations on this range of scales has slowed progress.

A major question is to partition the relative contributions of geostrophic eddies or inertia-gravity waves at the submesoscales, because they have different impact on dynamics and tracer transport (e.g. Callies & Ferrari 2013, hereafter CF13). A turbulent field of geostrophic eddies tends to transfer energy to larger scales and mix tracers along density surfaces. Internal wave interactions, instead, transfer energy to smaller vertical-scale waves, which break and mix tracers across density surfaces. In situ mooring observations are useful to separate sub-inertial and super-inertial motions, but the lack of spatial information prevents any conclusive statement about whether the sub-inertial motions are submesoscale geostrophic eddies or larger-scale motions and whether the super-inertial motions are inertia-gravity waves or other forms of stratified turbulence. Two dimensional sections (along ship tracks and depth) of velocity and density provide snapshots of the superposition of all submesoscale motions with no temporal information to separate the relative contributions. Maps of potential vorticity (PV) could be used to distinguish the two classes of motion, because geostrophic eddies are associated with PV anomalies whilst inertia-gravity waves have no PV signature. But PV requires three dimensional sections and it is extremely difficult to measure accurately (e.g. Müller *et al.* 1988).

CF13 used the fact that the ratio of the power spectra of along and across ship track velocities can be used to determine whether a velocity field is horizontally nondivergent, a necessary condition for flows to be in geostrophic balance. In this sense the geostrophic flow left a clear fingerprint in the observed horizontal velocities that could be tracked down. However, the horizontal velocity field due to inertia-gravity waves has both rotational and divergent components, so its fingerprint in the observed fields is not so immediately apparent.

In this work, we present a two-step method that allows extracting the fingerprint of inertia-gravity waves from ship track spectra. First, we show that measurements of the

two horizontal velocity components along ship tracks are sufficient to partition the flow uniquely into rotational (i.e. horizontally nondivergent) and divergent (i.e. horizontally irrotational) components, provided one can assume that the two fields are horizontally homogeneous and isotropic at the measured scales, and that their rotational and divergent components are uncorrelated in a statistical sense. This Helmholtz decomposition of the one-dimensional velocity spectra is purely kinematic in nature and is achieved by solving two simple ODEs in spectral space, an easy numerical task. We have not been able to find a direct prior reference in the literature for this kind of exact Helmholtz decomposition method for one-dimensional spectra, although related theoretical investigations do exist as in Lindborg (2007).

Specifically, in that paper it was shown how the one-dimensional covariances of vertical vorticity  $v_x - u_y$  and of horizontal divergence  $u_x + v_y$  can be expressed in terms of the one-dimensional horizontal velocity covariances by applying a certain second-order differential operator. This information can then be converted into the corresponding power spectra by Fourier transforms, which in principle also enables a Helmholtz decomposition of the horizontal flow because the vertical vorticity governs the rotational component and the horizontal divergence governs the divergent component. In practice, this depends on the smoothness of the observed covariance functions, which need to be differentiated twice in order to extract the flow components. This is a difficult task on noisy data and in the practical application of the theory to air flight data in Lindborg (2007) a parametric fit to an assumed shape of a piecewise defined covariance function is used instead. The Fourier transforms are then approximated by transforming each piecewise part of the covariance functions in isolation. In contrast, the decomposition technique derived in the present paper works directly on the power spectra of the observed fields and involves only integrals in spectral space, so no derivatives of noisy data need to be taken. This also allows our method to be applied directly to the data, without assuming any particular shape for the covariance functions.

Second, we show that for hydrostatic and vertically homogeneous inertia–gravity waves the aforementioned Helmholtz decomposition in combination with a statement about wave energy equipartition is sufficient to compute the one-dimensional wave energy spectrum. If buoyancy spectra are also available then this means that the total observed energy spectrum can be exactly decomposed into its inertia–gravity wave component and its residual vortical component in geostrophic balance. We also show that one can derive additional relationships between the power spectra if one has some information about the frequency content of the wave field (for example that it is narrow band, or that it follows a simple model spectrum). In this case it is possible to decompose not just the total observed energy spectrum but also the individual observed field spectra into their balanced and unbalanced components. This allows a complete decomposition of the one-dimensional spectra into their wave and vortex components, which is of obvious dynamical significance.

In section 2, we introduce the Helmholtz decomposition method for separating the rotational and divergent components of a two-dimensional velocity field from one dimensional spectra. Then we show how to determine what part of the spectrum is composed of inertia–gravity waves. Throughout, we consider only a very simple fluid set-up, which is a three-dimensional Boussinesq model with constant Coriolis parameter  $f$  and buoyancy frequency  $N$ . In section 3, the method is applied to ship based measurements of the upper ocean velocity field from two field experiments, one in the eastern subtropical North Pacific and one in the western North Atlantic. Despite noisy data and restrictive assumptions, in both cases the separation of submesoscale geostrophic motions from inertia–gravity waves appears to be fully successful.

## 2. Helmholtz decomposition and wave diagnostics

We begin by assembling some generic facts about one-dimensional velocity spectra that derive from a two-dimensional horizontal flow with homogeneous and isotropic statistics. For horizontally nondivergent flows this is a subset of well-known results from homogeneous turbulence theory, but for inertia-gravity waves we need to accommodate horizontal velocity fields that have both rotational and divergent components, which is a less studied case.

### 2.1. Helmholtz decomposition of one-dimensional spectra

Let  $u$  and  $v$  be horizontal velocity components defined in the  $xy$ -plane with  $x$  aligned with the ship track, so  $u$  is the along-track, “longitudinal” component and  $v$  is the across-track, “transverse” component. The time  $t$  and depth  $z$  are considered fixed during the measurement, so we may ignore these coordinates at this stage. If the flow is purely rotational, i.e. horizontally nondivergent, then  $(u, v)$  derive from a stream function  $\psi(x, y)$  in the standard way:

$$u_x + v_y = 0 \quad \Rightarrow \quad u = -\psi_y \quad \text{and} \quad v = +\psi_x. \quad (2.1)$$

Let  $\psi$  be a homogeneous and isotropic zero-mean random function such that

$$\mathbb{E}[\psi] = 0 \quad \text{and} \quad C^\psi(x, y) = \mathbb{E}[\psi(x_0, y_0)\psi(x_0 + x, y_0 + y)] = F(r) \quad (2.2)$$

where  $r = \sqrt{x^2 + y^2}$  and  $\mathbb{E}$  denotes taking the expected value. The function  $F(r)$  is the covariance of the stream function, which is a function of horizontal distance  $r \geq 0$  in the two-dimensional plane and encapsulates all the statistical knowledge that is available for the random velocity field. The power spectrum  $\hat{C}^\psi(k, l)$  is the Fourier transform of  $C^\psi(x, y)$ , i.e.

$$\hat{C}^\psi(k, l) = \int_{-\infty}^{\infty} \int_{-\infty}^{\infty} C^\psi(x, y) e^{-i(kx+ly)} dx dy = 2\pi \int_0^{\infty} J_0(k_h r) F(r) r dr = \hat{F}(k_h) \quad (2.3)$$

where  $k_h = \sqrt{k^2 + l^2}$ . The corresponding velocity spectra follow from (2.1) as

$$\hat{C}^u(k, l) = l^2 \hat{C}^\psi(k, l) = l^2 \hat{F}(k_h) \quad \text{and} \quad \hat{C}^v(k, l) = k^2 \hat{C}^\psi(k, l) = k^2 \hat{F}(k_h). \quad (2.4)$$

These are clearly not isotropic even though  $\hat{C}^\psi$  is. For completeness, the cross-spectrum

$$\hat{C}^{uv}(k, l) = -kl \hat{C}^\psi(k, l) = -kl \hat{F}(k_h). \quad (2.5)$$

Now, along the ship track  $y = 0$  and  $r = x$ , so the relevant one-dimensional covariance functions are given by  $C^\psi(x, 0) = F(x)$ , for example. For the power spectra this corresponds to integrating over the transverse wavenumber  $l$ :

$$\hat{C}^r(k) = \frac{1}{2\pi} \int_{-\infty}^{\infty} \hat{C}^\psi(k, l) dl = \frac{1}{2\pi} \int_{-\infty}^{\infty} \hat{F}(k_h) dl. \quad (2.6)$$

This integrand is even in  $l$  and, at fixed  $k$ , we have  $l dl = k_h dk_h$ , which allows rewriting (2.6) as

$$\hat{C}^r(k) = \frac{1}{\pi} \int_{|k|}^{\infty} \frac{\hat{F}(k_h)}{\sqrt{k_h^2 - k^2}} k_h dk_h. \quad (2.7)$$

The same steps lead to the one-dimensional velocity spectra

$$\psi \text{ only: } \hat{C}^u(k) = \frac{1}{\pi} \int_{|k|}^{\infty} \hat{F}(k_h) \sqrt{k_h^2 - k^2} k_h dk_h \quad (2.8)$$

$$\hat{C}^v(k) = \frac{k^2}{\pi} \int_{|k|}^{\infty} \frac{\hat{F}(k_h)}{\sqrt{k_h^2 - k^2}} k_h dk_h, \quad (2.9)$$

where “ $\psi$  only” is added as a reminder that these expressions hold only for horizontally nondivergent flows that can be expressed through a stream function  $\psi$ . The corresponding cross-spectrum  $\hat{C}^{uv}(k) = 0$ , because the relevant symbol  $kl$  in (2.5) is odd in  $l$  and hence integrates to zero. This will always be the case, so we won't consider the cross-spectrum any further. By inspection, and using Leibniz's rule, we obtain the celebrated formula

$$\psi \text{ only: } \hat{C}^v(k) = -k \frac{d}{dk} \hat{C}^u(k) \quad (2.10)$$

for the horizontally nondivergent case (e.g. Charney 1971). For power-law velocity spectra of the form  $k^{-n}$  this yields

$$\psi \text{ only: } \hat{C}^v(k) = n \hat{C}^u(k), \quad (2.11)$$

which, for  $n > 1$ , means that along a ship track the transverse spectrum dominates the longitudinal spectrum for two-dimensional incompressible flows. This is the fingerprint that was exploited in CF13.

Conversely, we may consider a purely divergent flow, i.e. one that is two-dimensionally irrotational such that (2.1) is replaced by

$$v_x - u_y = 0 \quad \Rightarrow \quad u = \phi_x \quad \text{and} \quad v = \phi_y \quad (2.12)$$

in terms of a homogeneous and isotropic zero-mean random potential  $\phi(x, y)$  defined by

$$\mathbb{E}[\phi] = 0 \quad \text{and} \quad C^\phi(x, y) = \mathbb{E}[\phi(x_0, y_0)\phi(x_0 + x, y_0 + y)] = G(r), \quad (2.13)$$

where  $G(r)$  is the covariance of  $\phi$ . Clearly, apart from the sign change, this simply reverses the roles of  $u$  and  $v$  in (2.1), so all the spectra can be worked out just as before. For the two-dimensional spectra this yields

$$\hat{C}^u(k, l) = k^2 \hat{G}(k_h) \quad \text{and} \quad \hat{C}^v(k, l) = l^2 \hat{G}(k_h) \quad (2.14)$$

and the one-dimensional ship track spectra are

$$\phi \text{ only: } \hat{C}^u(k) = \frac{k^2}{\pi} \int_{|k|}^{\infty} \frac{\hat{G}(k_h)}{\sqrt{k_h^2 - k^2}} k_h dk_h \quad (2.15)$$

$$\hat{C}^v(k) = \frac{1}{\pi} \int_{|k|}^{\infty} \hat{G}(k_h) \sqrt{k_h^2 - k^2} k_h dk_h, \quad (2.16)$$

where “ $\phi$  only” is added as a reminder that these expressions hold only for irrotational flows that can be expressed through a velocity potential  $\phi$ . The relationship (2.10) is replaced by

$$\phi \text{ only: } \hat{C}^u(k) = -k \frac{d}{dk} \hat{C}^v(k) \quad (2.17)$$

and hence now the longitudinal spectrum dominates for power laws with  $n > 1$ :

$$\phi \text{ only: } \hat{C}^u(k) = n \hat{C}^v(k). \quad (2.18)$$

Note that by definition both  $\hat{F}$  and  $\hat{G}$  are real and non-negative functions of  $k_h$ .

Now, a general two-dimensional flow has a Helmholtz decomposition into rotational and divergent components of the form

$$u = -\psi_y + \phi_x \quad \text{and} \quad v = \psi_x + \phi_y, \quad (2.19)$$

which implies the two-dimensional Poisson equations

$$\psi_{xx} + \psi_{yy} = v_x - u_y \quad \text{and} \quad \phi_{xx} + \phi_{yy} = u_x + v_y. \quad (2.20)$$

This determines both  $\psi$  and  $\phi$  up to a harmonic function, but with doubly periodic boundary conditions such a harmonic function could only be a physically meaningless constant, so  $\psi$  and  $\phi$  are in fact uniquely determined by (2.20). Progress with the statistical theory is then possible if  $\psi(x, y)$  and  $\phi(x, y)$  are uncorrelated in the sense that

$$\mathbb{E}[\psi(x_0, y_0)\phi(x_0 + x, y_0 + y)] = 0 \quad (2.21)$$

holds for all  $(x, y)$ . Under this assumption the velocity covariances due to  $\psi$  and  $\phi$  simply add up, which yields the one-dimensional ship track spectra

$$\hat{C}^u(k) = \frac{1}{\pi} \int_{|k|}^{\infty} \left[ \hat{F}(k_h) \sqrt{k_h^2 - k^2} + \frac{k^2 \hat{G}(k_h)}{\sqrt{k_h^2 - k^2}} \right] k_h dk_h \quad (2.22)$$

$$\hat{C}^v(k) = \frac{1}{\pi} \int_{|k|}^{\infty} \left[ \frac{k^2 \hat{F}(k_h)}{\sqrt{k_h^2 - k^2}} + \hat{G}(k_h) \sqrt{k_h^2 - k^2} \right] k_h dk_h. \quad (2.23)$$

These expressions can be substantially simplified if one introduces the auxiliary functions  $D^\psi(k)$  and  $D^\phi(k)$  defined by

$$D^\psi(k) = \frac{1}{2\pi} \int_{-\infty}^{\infty} l^2 \hat{C}^\psi(k, l) dl = \frac{1}{\pi} \int_{|k|}^{\infty} \hat{F}(k_h) \sqrt{k_h^2 - k^2} k_h dk_h \quad (2.24)$$

$$D^\phi(k) = \frac{1}{2\pi} \int_{-\infty}^{\infty} l^2 \hat{C}^\phi(k, l) dl = \frac{1}{\pi} \int_{|k|}^{\infty} \hat{G}(k_h) \sqrt{k_h^2 - k^2} k_h dk_h, \quad (2.25)$$

The functions  $D^\psi$  and  $D^\phi$  are the spectra of  $\psi_y$  and  $\phi_y$ , respectively, and they allow rewriting (2.22-2.23) in the succinct form

$$\hat{C}^u(k) = D^\psi(k) - k \frac{d}{dk} D^\phi(k) \quad \text{and} \quad \hat{C}^v(k) = D^\phi(k) - k \frac{d}{dk} D^\psi(k). \quad (2.26)$$

This is the main result of this section, which neatly incorporates both (2.10) and (2.17) as special cases. The functions  $D^\psi$  and  $D^\phi$  can be viewed as analogous to  $\psi$  and  $\phi$  in the Helmholtz decomposition of the ship track velocity spectra. Correspondingly, the horizontal kinetic energy spectrum can be viewed as the sum of a rotational and a divergent part:

$$\frac{1}{2} [\hat{C}^u(k) + \hat{C}^v(k)] = \frac{1}{2} \left[ D^\psi(k) - k \frac{d}{dk} D^\psi(k) \right] + \frac{1}{2} \left[ D^\phi(k) - k \frac{d}{dk} D^\phi(k) \right]. \quad (2.27)$$

## 2.2. Numerical method for Helmholtz decomposition

The spectral functions  $D^\psi(k)$  and  $D^\phi(k)$  are not directly observable from the ship track data, but (2.26) suggests a simple and robust method for computing them from the directly observed  $\hat{C}^u$  and  $\hat{C}^v$ . First, the functions  $D^\psi$  and  $D^\phi$  are symmetric in  $k$  so we only need to find their values for  $k \geq 0$ . Second, in the limit  $k \rightarrow \infty$  we have the robust

decay boundary conditions

$$D^\psi(+\infty) = D^\phi(+\infty) = 0 \quad (2.28)$$

and this allows us to compute  $D^\psi$  and  $D^\phi$  for  $k \geq 0$  by integrating the two ODEs in (2.26) backwards in  $k$ , starting from zero values at  $k = +\infty$ . This is particularly easy in the logarithmic wavenumber

$$s = \ln k \quad \text{such that} \quad \frac{d}{ds} = k \frac{d}{dk}. \quad (2.29)$$

The ODEs in (2.26) can be integrated numerically, but there is also a closed-form solution

$$D^\psi(s) = \int_s^\infty \left[ \hat{C}^u(\bar{s}) \sinh(s - \bar{s}) + \hat{C}^v(\bar{s}) \cosh(s - \bar{s}) \right] d\bar{s} \quad (2.30)$$

$$D^\phi(s) = \int_s^\infty \left[ \hat{C}^u(\bar{s}) \cosh(s - \bar{s}) + \hat{C}^v(\bar{s}) \sinh(s - \bar{s}) \right] d\bar{s}. \quad (2.31)$$

In this formulation, the functions  $D^\psi$  and  $D^\phi$  at wavenumber  $k$  only depend on the velocity spectra at wavenumbers larger than  $k$ , which is consistent with the aliasing apparent in their definition in (2.24). Notably, the  $\sinh(s - \bar{s})$  terms in (2.30) and (2.31) are negative, which can lead to unphysical negative values in  $D^\psi$  or  $D^\phi$ . This may occur when either  $D^\psi$  or  $D^\phi$  become very small, say comparable to the instrumental noise threshold or to the errors imposed by the limitations of the assumptions of isotropy and homogeneity in the data (cf. § 3.2 below).

### 2.3. Inertia–gravity waves and the wave energy spectrum

We now consider the linear Boussinesq equations with constant  $f$  and  $N$  in a domain with doubly periodic horizontal boundary conditions. The horizontal velocity field induced by linear inertia–gravity waves then has both a stream function and a velocity potential component, which are related as follows. The vertical vorticity satisfies the linear equation

$$(v_x - u_y)_t = fw_z = -f(u_x + v_y) \quad \Rightarrow \quad \psi_t + f\phi = 0. \quad (2.32)$$

Equation (2.32) shows that  $\psi$  and  $\phi$  are in quadrature in time, which we will take to imply that for a stationary and horizontally isotropic field of random waves  $\psi$  and  $\phi$  are uncorrelated at any fixed time  $t$ , and therefore the key assumption (2.21) indeed holds for linear inertia–gravity waves. The reasoning behind this is described in appendix 5.1.

It is of course possible to define further spectral relationships based on the linear equations, for example (2.32) implies the frequency-dependent relationship

$$\hat{C}_W^\psi(k, l, \omega) = \frac{f^2}{\omega^2} \hat{C}_W^\phi(k, l, \omega) \quad (2.33)$$

between the three-dimensional wave spectra of  $\psi$  and  $\phi$ , which are defined in the usual way as functions of the horizontal wavenumbers and the wave frequency. (Here and in the following we denote wave-related functions by the subscript  $W$ .) However, such relationships include the wave frequency  $\omega$  as a parameter, which depends on  $(k, l)$  but also on the vertical wavenumber or some other information about the vertical structure of the waves. This is of limited use for general ship track observations, where the vertical structure is typically not known and therefore (2.33) cannot be reduced to a unique statement for two-dimensional or one-dimensional spectra. We note in passing that the situation would be very different in a two-dimensional fluid system such as the shallow-water equations, where the dispersion relation determines  $\omega^2$  as a function of  $(k, l)$ . In

this case (2.33) would indeed hold for the two-dimensional spectra, with  $\omega^2$  determined from the dispersion relation.

We will therefore pursue a different course of action under the assumption that the waves are *hydrostatic*, implying that the vertical velocity is negligible in the wave energy budget. Somewhat surprisingly, this assumption will allow us to deduce the exact one-dimensional wave energy spectrum

$$E_W(k) = \frac{1}{2} \left[ \hat{C}_W^u(k) + \hat{C}_W^v(k) + \hat{C}_W^b(k) \right] \quad (2.34)$$

solely from ship track observations of  $u$  and  $v$ ! Here  $\hat{C}_W^b(k)$  is the spectrum of  $b/N$  where  $b$  is the linear buoyancy disturbance, which is related to the vertical velocity  $w$  by

$$b_t + N^2 w = 0. \quad (2.35)$$

Hence  $\frac{1}{2}\hat{C}_W^b$  is the potential energy spectrum. The computation of  $E_W(k)$  in (2.34) hinges on the following statement about the energy equipartition for linear hydrostatic inertia–gravity waves that are stationary in time as well as spatially homogeneous in all three directions: the sum of the potential energy plus the rotational horizontal kinetic energy due to  $\psi$  then equals the divergent horizontal kinetic energy due to  $\phi$ . This statement is derived in appendix 5.2 and using (2.27) it takes the form

$$\hat{C}_W^b(k) + \left[ D_W^\psi(k) - k \frac{d}{dk} D_W^\psi(k) \right] = \left[ D_W^\phi(k) - k \frac{d}{dk} D_W^\phi(k) \right]. \quad (2.36)$$

Substitution in (2.34) then immediately yields the key result

$$E_W(k) = D_W^\phi(k) - k \frac{d}{dk} D_W^\phi(k). \quad (2.37)$$

In a nutshell, this equation asserts that a Helmholtz decomposition of the horizontal velocity spectra along a ship track yields the exact wave energy spectrum of linear hydrostatic inertia–gravity waves, at least under the assumption that the waves can be modelled as spatially homogeneous, including in the vertical. For a wave field dominated by low-order vertical modes this latter assumption would fail, but otherwise the generality of (2.37) is remarkable. We note in passing that (2.36) is the hydrostatic version of a more general equipartition statement (5.9) that is also derived in appendix 5.2. However, this more general statement involves the spectrum of the vertical velocity component, which is typically not available in present-day observations.

#### 2.4. Combination with a geostrophic flow component

If the inertia–gravity wave field is embedded in a vortical flow in geostrophic balance then the horizontal velocity field can be viewed as the sum of an unbalanced wave part and of a balanced ‘vortex’ part. We allow for this by extending the Helmholtz decomposition to

$$\psi = \psi_W + \psi_V \quad \text{and} \quad \phi = \phi_W, \quad (2.38)$$

where the subscript  $V$  denotes the vortex part. The vortex part is horizontally non-divergent and therefore  $\phi$  has no vortex part.

It is reasonable on physical grounds to assume that  $\psi_V$  is statistically independent of  $\psi_W$  and  $\phi_W$ , in which case the covariances due to  $\psi_V$  simply add to the wave covariances we have already considered, i.e.,

$$\hat{C}^u(k) = \hat{C}_W^u(k) + \hat{C}_V^u(k) \quad \text{and} \quad \hat{C}^v(k) = \hat{C}_W^v(k) + \hat{C}_V^v(k). \quad (2.39)$$



The corresponding Helmholtz decomposition leads to

$$D^\psi(k) = D_W^\psi(k) + D_V^\psi(k) \quad \text{and} \quad D^\phi(k) = D_W^\phi(k) \quad (2.40)$$

such that

$$\hat{C}_W^u(k) = D_W^\psi(k) - k \frac{d}{dk} D_W^\phi(k), \quad \hat{C}_W^v(k) = -k \frac{d}{dk} D_W^\psi(k) + D_W^\phi(k) \quad (2.41)$$

$$\hat{C}_V^u(k) = D_V^\psi(k), \quad \hat{C}_V^v(k) = -k \frac{d}{dk} D_V^\psi(k). \quad (2.42)$$

Crucially,  $D_W^\phi = D^\phi$  can be computed from the observed velocity spectra exactly as before, i.e., the function  $D_W^\phi$  computed from the velocity observations is unaffected by the geostrophic flow component. The same is hence true for the hydrostatic wave energy spectrum  $E_W$  computed in (2.37). In other words, allowing for the presence of a geostrophic stream function does not affect the method of computation of the wave energy spectrum at all, because the crucial potential part of the Helmholtz decomposition of the spectra is not affected by the geostrophic flow.

At this point  $E_W$ ,  $D^\phi = D_W^\phi$  and the sum  $D^\psi = D_W^\psi + D_V^\psi$  are known, but not  $D_W^\psi$  and  $D_V^\psi$  individually. So the vortical energy spectrum as well as the individual wave and vortex velocity spectra in (2.41–2.42) are still unknown. Either additional assumptions or additional observations are needed to progress further. We consider two options: either observing  $b/N$  along the ship track, or assuming additional information about the frequency content of the wave field.

### 2.5. Observed buoyancy spectrum

If  $b/N$  is observed along the ship track then we know the potential energy spectrum  $\frac{1}{2}\hat{C}^b$  and hence also the total energy spectrum

$$E(k) = E_W(k) + E_V(k) = \frac{1}{2} \left[ \hat{C}^u(k) + \hat{C}^v(k) + \hat{C}^b(k) \right]. \quad (2.43)$$

Now, because  $E_W$  can be computed from (2.37), the vortical energy spectrum

$$E_V(k) = \frac{1}{2} \left[ \hat{C}_V^u(k) + \hat{C}_V^v(k) + \hat{C}_V^b(k) \right] = E(k) - E_W(k) \quad (2.44)$$

simply follows by subtraction, so we now know both  $E_W$  and the residual  $E_V$ . This provides an exact energy decomposition into wave and vortex parts based solely on observing  $(u, v, b/N)$  along a ship track, which is of obvious physical importance.

On the other hand, it is still not possible to compute the spectra of the individual wave and vortex fields from the available data. For example,  $\hat{C}^b$  is known but not its constituents  $\hat{C}_W^b$  and  $\hat{C}_V^b$ . At least one further auxiliary assumption would be needed to overcome this. For example, in Charney's conception of energy equipartition in three-dimensional quasi-geostrophic turbulence with isotropic statistics (after rescaling the vertical coordinate by  $f/N$ ) (Charney 1971), the vortical buoyancy spectrum is approximately equal to the longitudinal velocity spectrum, which in the present notation would imply

$$\hat{C}_V^b(k) = \hat{C}_V^u(k) = D_V^\psi(k). \quad (2.45)$$

Combining this with (2.44) and (2.42) yields

$$E_V(k) = D_V^\psi(k) - \frac{k}{2} \frac{d}{dk} D_V^\psi(k), \quad (2.46)$$

which is an ODE for  $D_V^\psi$  in terms of the known  $E_V$ . This is again easily solved for  $D_V^\psi(k)$

by starting with a zero value at  $k = +\infty$  and solving backwards in  $k$  for all  $k \geq 0$ . Thereafter  $D_W^\psi = D^\psi - D_V^\psi$  is known as well and hence all fields have been completely decomposed into their wave and vortex constituents. This is an attractive theoretical result, but it must be clearly noted that the underlying heuristic assumption (2.45) based on isotropy in rescaled coordinates may in practice hold only for the smallest scales of the geostrophic flow, if it holds at all. We will not use this approach in this paper.

### 2.6. Frequency models for the wave spectrum

Substantial progress can be made if one assumes a more detailed model for the frequency content of the wave spectrum. For example, if the wave field is narrow-banded in frequency then it makes sense to assign a single typical value to the parameter  $f^2/\omega^2$  that appears in relationships such as (2.33). If we denote this constant value by  $f^2/\omega_0^2$  then (2.33) implies the spectral relationships

$$\hat{C}_W^\psi(k, l) = \frac{f^2}{\omega_0^2} \hat{C}_W^\phi(k, l) \quad \text{and} \quad D_W^\psi(k) = \frac{f^2}{\omega_0^2} D^\phi(k). \quad (2.47)$$

With  $D_W^\psi$  and  $D_V^\psi = D^\psi - D_W^\psi$  now in hand we can evaluate all the terms in (2.41) and (2.42). Moreover,  $\hat{C}_W^b$  follows from the known  $E_W$  as

$$\hat{C}_W^b(k) = 2E_W(k) - \hat{C}_W^u(k) - \hat{C}_W^v(k). \quad (2.48)$$

This narrow-band approach for the wave spectrum might be relevant for inertia–gravity wave fields dominated by specific tidal components such as the M2 tide, but such internal tides also tend to be quite anisotropic.

A more flexible modelling approach extends the second equation in (2.47) to a function  $\omega_*(k)$ , say, which is *defined* by

$$D_W^\psi(k) = \frac{f^2}{\omega_*^2(k)} D^\phi(k). \quad (2.49)$$

Clearly, if  $\omega_*(k)$  is somehow known then one can again compute  $D_W^\psi$  from the observed  $D^\phi$  and hence again obtain the complete decomposition of the spectra into their wave and vortex constituents in (2.41–2.42). For ease of reference, in terms of  $D^\psi$  and  $D^\phi$  these relations become

$$\hat{C}_W^u(k) = \frac{f^2}{\omega_*^2(k)} D^\phi(k) - k \frac{d}{dk} D^\phi(k), \quad \hat{C}_W^v(k) = -k \frac{d}{dk} \left[ \frac{f^2}{\omega_*^2(k)} D^\phi(k) \right] + D^\phi(k) \quad (2.50)$$

$$\hat{C}_V^u(k) = D^\psi(k) - \frac{f^2}{\omega_*^2(k)} D^\phi(k), \quad \hat{C}_V^v(k) = -k \frac{d}{dk} \left[ D^\psi(k) - \frac{f^2}{\omega_*^2(k)} D^\phi(k) \right]. \quad (2.51)$$

Again,  $\hat{C}_W^b$  can then be computed from (2.48), which provides a “sight unseen” prediction for the buoyancy spectrum.

Of course, this only works if the function  $\omega_*(k)$  is known by some method, for example by using a model spectrum for the wave field to evaluate the definition of  $\omega_*(k)$  that follows from the exact three-dimensional spectral relationship between  $\hat{C}_W^\psi$  and  $\hat{C}_W^\phi$  in (2.33), namely

$$\frac{f^2}{\omega_*^2(k)} = \frac{D_W^\psi(k)}{D^\phi(k)} = \frac{\int \int \frac{f^2}{\omega^2} l^2 \hat{C}^\phi(k, l, \omega) dld\omega}{\int \int l^2 \hat{C}^\phi(k, l, \omega) dld\omega}. \quad (2.52)$$

For example, in the next section we will use the standard Garrett–Munk (GM) spectrum (e.g. Munk 1981) for ocean inertia–gravity waves as a basis for modelling the function  $\omega_*(k)$ . Notably,  $\omega_*(k)$  as defined by (2.52) is insensitive to the overall amplitude of the

wave spectrum. Alternatively, if the observed spectra are dominated by waves in some wavenumber band (i.e.,  $D^\psi \approx D_W^\psi$  there), then it is possible to estimate  $\omega_*(k)$  in that wavenumber band directly from its definition (2.49), with  $D_W^\psi$  approximated by  $D^\psi$ . This can provide a useful check on the validity of any assumed model spectrum, as we shall see in § 3.1 below.

### 2.7. Summary of the Helmholtz decomposition method

We can summarize the theoretical results as follows. Observations of the longitudinal and transverse velocity spectra  $\hat{C}^u$  and  $\hat{C}^v$  allow a unique Helmholtz decomposition in terms of the functions  $D^\phi$  and  $D^\psi$ . Moreover, the function  $D^\phi$  then implies the energy spectrum  $E_W$  for hydrostatic inertia–gravity waves, and this implication is unaffected by the presence of a geostrophic vortex flow component, provided only that this component is uncorrelated with the wave component. Additional observations of  $\hat{C}^b$  allow computation of the vortex energy spectrum  $E_V$  as well, which can then be compared with the wave energy spectrum  $E_W$ . Finally, by making additional assumptions either about the structure of the balanced flow or about the frequency content of the wave field, it becomes possible to decompose all measured fields into their wave and vortex components.

## 3. Application to oceanic data sets

We now illustrate how these methods can be used to decompose observed ship-track spectra in the upper thermocline of the eastern subtropical North Pacific and of the Gulf Stream region. These spectra, spanning the mesoscale (about 200–500 km) and submesoscale (about 5–200 km) ranges, are the same as those analyzed in CF13, to which we refer the reader for a more in-depth discussion of the data sets as well as of mesoscale and submesoscale dynamics.

In the eastern subtropical North Pacific, both velocity and buoyancy measurements are available, which allows an exact decomposition of the energy spectra into a balanced vortex part and an inertia–gravity wave part. Moreover, by approximating the function  $\omega_*(k)$  using the GM model spectrum, we can decompose all the observed fields into their balanced and wave parts. In the Gulf Stream region, on the other hand, only velocity data are available, but by assuming a GM model for  $\omega_*(k)$  a decomposition of the observed fields can be achieved there, too.

The eastern subtropical North Pacific has weak mesoscale eddy activity and CF13 argued that much of the submesoscale range is dominated by inertia–gravity waves. In the Gulf Stream region, on the other hand, where the mesoscale eddy field is strong, the submesoscale is dominated by balanced motions down to a scale of about 20 km, where a transition to inertia–gravity waves occurs. The decompositions performed here confirm these results.

### 3.1. Eastern subtropical North Pacific

Velocity and buoyancy data were collected in successive occupations of the 140°W meridian between 25° and 35°N in January and February 1997 (cf. Ferrari & Rudnick 2000, CF13). We use shipboard acoustic Doppler current profiler (ADCP) data from four transects at 200 m depth (8 m depth bin), which is below the base of the mixed layer. Buoyancy data are obtained from a transect of a CTD-equipped SeaSoar programmed to stay at constant depth 200 m. An average stratification of  $N = 8.7 \times 10^{-3} \text{ s}^{-1}$  is obtained from a transect with the SeaSoar following a sawtooth profile. We interpolate both velocity and buoyancy data onto a 3 km regular grid, which is about the spacing of the raw velocity data averaged over 12 min bins, and rotate the velocities into a frame of

reference aligned with the ship track. Spectra are obtained by dividing all transects into three segments with 50% overlap, applying a Hann window to each segment, computing the discrete Fourier transform, and averaging over all transforms and over 10 wavenumber bins per decade.

The resulting  $\hat{C}^u$ ,  $\hat{C}^v$ , and  $\hat{C}^b$  show relatively low mesoscale energies and are relatively flat in the submesoscale range (Fig. 1a). Using equations (2.30–2.31), we perform the Helmholtz decomposition into rotational and divergent components (Fig. 1b). The rotational component dominates at scales larger than 200 km, below which the divergent component dominates. From the velocity spectra  $\hat{C}^u$  and  $\hat{C}^v$ , we can diagnose the total energy due to inertia–gravity waves  $E_W$  using (2.37). The diagnosed  $E_W$  matches the observed total energy  $E$  remarkably well below 100 km (Fig. 1c). This indicates that the observed signal is consistent with an isotropic, hydrostatic inertia–gravity wave field in this range. At scales larger than 100 km there is a substantial balanced component.

We can exploit the fact that the range below 100 km is dominated by inertia–gravity waves to estimate the frequency content of the wave field expressed by  $\omega_*$ . The ratio  $D^\psi/D^\phi \approx f^2/\omega_*^2$  roughly follows the GM curve between 20 and 100 km (Fig. 1d). At larger scales the ratio becomes larger than unity, which is incompatible with inertia–gravity waves, for which  $\omega^2 \geq f^2$  holds robustly. At smaller scales, the diagnosed ratio is much larger than the GM value, but in this range the effects of both the interpolation onto a regular grid and the cutoff at the Nyquist wavenumber contaminate the estimate. At 100 km, the diagnosed ratio drops below the GM curve and has a value close to that of a monochromatic  $M_2$  tidal wave ( $f^2/\omega_0^2 = 0.27$  at  $30^\circ\text{N}$ ), which may be interpreted as evidence for a significant tidal signal at this scale. Nevertheless using the GM curve to perform the decomposition (2.48, 2.50, 2.51), we find that the balanced components  $\hat{C}_V^u$ ,  $\hat{C}_V^v$ , and  $\hat{C}_V^b$  match the observed spectra  $\hat{C}^u$ ,  $\hat{C}^v$ , and  $\hat{C}^b$  at scales larger than 200 km (Fig. 1e) and that the inertia–gravity waves components  $\hat{C}_W^u$ ,  $\hat{C}_W^v$ , and  $\hat{C}_W^b$  match the observed spectra  $\hat{C}^u$ ,  $\hat{C}^v$ , and  $\hat{C}^b$  at scales smaller than 100 km (Fig. 1f).

In summary, kinetic and potential energy spectra are dominated by balanced eddies at scales of 200 km and larger. This is consistent with CF13’s finding that at these scales, the in situ  $\hat{C}^v$  also matches that obtained from applying geostrophic balance to along-track altimetric measurements of sea surface height. At scales smaller than 100 km, the energy spectra are dominated by inertia–gravity waves. The inertia–gravity wave field may have a substantial tidal component.

### 3.2. Gulf Stream region

Velocity data in the Gulf Stream region were collected using a 150 kHz shipboard ADCP on repeat transects from New York Harbor to Bermuda between 1994 and 2004 (cf. Wang *et al.* 2010, CF13). We use data at 150-m depth, which is below the base of the mixed layer in most of the year. We select transects that are at least 1000 km long and have at least 400 data points, resulting in a total of 306 transects. We interpolate onto a 2.5 km regular grid, which is about the spacing of the raw data averaged over 5 min bins, and rotate the velocities into a frame of reference aligned with the ship track. Spectra are obtained by the same procedure as described for the Pacific data set.

The resulting  $\hat{C}^u$  and  $\hat{C}^v$  show large mesoscale energies and fall off steeply in the submesoscale range (Fig. 2a). The spectra exhibit a conspicuous flattening at a scale of about 20 km. Using equations (2.30–2.31), we perform the Helmholtz decomposition into rotational and divergent components (Fig. 1b). In contrast to the eastern Pacific case, the rotational part  $D^\psi$  here vastly dominates over a wide range of scales: only at 20 km does the divergent component  $D^\phi$  become comparable to the rotational component  $D^\psi$ .

Notably, at large scales the true  $D^\phi$  becomes close to zero, but our computed  $D^\phi$  actually becomes negative, which is of course unphysical. This is the numerical robustness issue discussed at the end of 2.2.

Since no buoyancy data are available, the only way to decompose into a balanced part and an inertia–gravity wave part is to make an assumption about the frequency content of the waves. We choose the GM curve to perform the decomposition, since the GM empirical spectrum is largely based on observations collected nearby the North Atlantic region considered here. The diagnosed balanced components  $\hat{C}_V^u$  and  $\hat{C}_V^v$  show good agreement with the observed spectra  $\hat{C}^u$  and  $\hat{C}^v$  in the range 50–200 km (Fig. 2c). At larger scales, the reconstruction overestimates the longitudinal component  $\hat{C}^u$ . This is likely the effect of anisotropy in the flow: the Gulf Stream, running mostly transverse to the ship track, has scales of a few hundred kilometers and renders the geostrophic flow field highly anisotropic (cf. Wortham *et al.* 2014), violating the isotropy assumption made throughout the development of the theory. At the small-scale end, the balanced components  $\hat{C}_V^u$  and  $\hat{C}_V^v$  start deviating from the observed spectra  $\hat{C}^u$  and  $\hat{C}^v$  at 20–50 km. This scale is coincident with the scale at which the observed spectra  $\hat{C}^u$  and  $\hat{C}^v$  start flattening out. The balanced components  $\hat{C}_V^u$  and  $\hat{C}_V^v$  show no sign of a transition and keep falling off steeply. The diagnosed inertia–gravity wave components  $\hat{C}_W^u$  and  $\hat{C}_W^v$  start contributing substantially at this scale (Fig. 2d), indicating that the flattening of the spectra  $\hat{C}^u$  and  $\hat{C}^v$  is due to a transition to a range dominated by inertia–gravity waves.

In summary, the decomposition into a balanced part and an inertia–gravity wave part shows that in the Gulf Stream region, in contrast to the eastern Pacific case, much of the submesoscale range is dominated by balanced flows. The transition in the slope of the observed spectra at about 20 km is due to inertia–gravity waves.

#### 4. Concluding comments

Our proposed method is very easy to implement and gave robust results when applied to real oceanic data sets, in the sense that no processing of the noisy raw data was needed in order to extract a self-consistent picture of the partitioning into rotational and divergent motions and into waves and vortices. Of course, there are several restrictions inherent in the derivation of our method, which one needs to bear in mind. The assumptions of stationarity, homogeneity, and horizontal isotropy will have obvious limitations in any practical situation. Another obvious restriction that is hindering in practice is that we needed to assume that the wave field was homogeneous in the vertical in order to exploit the energy equipartition result (2.36) for the wave diagnostic. Strictly speaking, this step disallows considering standing normal modes in the vertical, which is a relevant case for large-scale ocean inertia–gravity waves such as low-mode internal tides. Another useful extension would be to allow for a depth-dependent buoyancy frequency  $N$ , which again would break the vertical homogeneity assumption and also would require the consideration of suitable vertical modes.

Slightly less obvious will be the impact of nonlinear effects, as our method relied on geostrophic balance and linear waves dynamics. For example, the assumption of uncorrelated  $\psi$  and  $\phi$ , which underlies both steps in our method, presumably would fail for vortex motions with a noticeable divergent component (the so-called ‘ageostrophic’ velocities of quasi-geostrophic theory). Submesoscale balanced flows tend to develop a large divergence close to the ocean surface through frontogenesis (CF13). It is not obvious

what this would entail for the correlations between the rotational and divergent parts of the balanced velocity field.

Similarly, nonlinear effects would also modify the linear argument for the uncorrelated  $\psi$  and  $\phi$  for the wave field. That argument can be viewed as a statement of zero linear PV, or of stretching of background vorticity, in the sense of  $v_x - u_y = -fb_z/N^2$ . In nonlinear theory one could imagine that nonlinear terms in the definition of PV become important, and that the stretching of background vorticity might reasonably contain a contribution from the vorticity of the geostrophic flow. A model equation for the wave vorticity to study in a weakly nonlinear regime might be

$$(\partial_{xx}^2 + \partial_{yy}^2)\partial_t\psi_W = [f + (\partial_{xx}^2 + \partial_{yy}^2)\psi_V](\partial_{xx}^2 + \partial_{yy}^2)\phi_W. \quad (4.1)$$

Compared to (2.32) this includes a nonlinear coupling term between  $\psi_V$  and the wave-related  $\psi_W$  and  $\phi_W$ . Of course, in a strongly nonlinear regime one would also encounter stratified turbulence, a broad subject heading describing three-dimensionally turbulent flows that are significantly modified by, and interact with, the stable stratification (e.g. Smith & Waleffe 2002; Waite & Bartello 2004; Riley & Lindborg 2008). It is an open question whether such stratified turbulence, perhaps also modified by background rotation, would leave a detectable fingerprint in the one-dimensional spectra that would allow distinguishing it from the spectrum due to nearly linear waves, for example.

Finally, our method should naturally be applicable to the substantial body of commercial air flight track data that has been collected near the tropopause in the atmosphere, where attention has been focused for some time on disentangling the dynamical processes that underlie the conspicuous transitions between spectral slopes that have been observed in the so-called Gage–Nastrom spectrum (e.g. Nastrom & Gage 1985; Lindborg 1999; Tulloch & Smith 2006). We are hoping to report on the results of this application in the near future.

OB thanks Miranda Holmes–Cerfon for interesting discussions and gratefully acknowledges financial support under grants CMG-1024180, DMS-1312159, and DMS-1009213 of the United States National Science Foundation. JC and RF thank Glenn Flierl for offering useful feedbacks during the preparation of the manuscript and acknowledge financial support under grants N-00014-09-1-0458 and GMG-1024198.

## 5. Appendix

### 5.1. *Horizontally uncorrelated wave stream function and potential*

We seek to demonstrate that

$$(2.21) : \quad \mathbb{E}[\psi(x_0, y_0, z_0, t_0)\phi(x_0 + x, y_0 + y, z_0, t_0)] = 0$$

holds if the expectation is taken over a stationary, homogeneous, and horizontally isotropic wave spectrum, and if  $\psi$  and  $\phi$  are wave fields related by a time derivative, as in the relation  $\psi_t = -f\phi$  that holds for inertia–gravity waves. Here we rewrote (2.21) in a form that highlights that the covariance is taken at different horizontal positions but equal vertical position  $z_0$  and time  $t_0$ . By stationarity, the statement (2.21) is trivially true in the case of  $x = y = 0$ , but not otherwise.

We will illustrate this issue using a slightly simpler model, namely the rotating shallow-water in one spatial dimension  $x$ , say, in which horizontal isotropy is replaced by left–right symmetry. The standard variables are  $(h, u, v)$  and the linear equations are

$$u_t - fv + gh_x = 0, \quad v_t + fu = 0, \quad \text{and} \quad h_t + Hu_x = 0, \quad (5.1)$$

where  $g$  is gravity and  $H$  is the basic layer depth. Note that  $u$  and  $v$  are in quadrature because of the time derivative linking the two fields in (5.1), just as  $\phi$  and  $\psi$  were in the inertia–gravity wave case. The fields depend on  $x$  and  $t$  and we assume stationarity and homogeneity. We then like to find out whether

$$\mathbb{E}[u(x_0, t_0)v(x_0 + x, t_0)] = 0 \tag{5.2}$$

holds for left–right symmetric waves. Now, it is easy to construct a homogeneous and stationary spectrum for which (5.2) fails. Specifically, consider this spectrum of plane-wave solutions corresponding to right-going waves only:

$$u = \beta \cos(k[x - ct] - \alpha), \quad v = \frac{f}{ck} \beta \sin(k[x - ct] - \alpha), \quad \text{and} \quad h = \frac{H}{c} \beta \cos(k[x - ct] - \alpha). \tag{5.3}$$

Here  $k > 0$  is a wavenumber,  $c = \omega/k > 0$  is the phase speed corresponding to the positive root of the dispersion relation  $\omega^2 = f^2 + gHk^2$ ,  $\alpha \in [0, 2\pi]$  is a uniformly distributed random phase shift and  $\beta$  is a random zero-mean amplitude that is independent of  $\alpha$  and has variance  $\sigma^2$ , say. It follows that

$$\mathbb{E}[u(x_0, t_0)v(x_0 + x, t_0)] = \frac{f}{ck} \sigma^2 \sin kx, \tag{5.4}$$

where it was crucial to take the expectation over the random phase shift  $\alpha$ . Obviously, for this random wave field (5.2) failed. However, if we impose left–right symmetry on the random wave field then we must augment (5.3) by a second wave with identical and uncorrelated statistics, but going in the opposite direction. This corresponds to setting  $c = -\omega/k < 0$  and obviously uses the other branch of the dispersion relation. This leads to a second term in (5.4) with equal-and-opposite sign, which cancels the first term, and therefore (5.2) is indeed satisfied.

The conclusion is that for wave systems with equal-and-opposite frequency branches in the dispersion relation a horizontally isotropic stationary random wave field has the property that (2.21) is guaranteed to hold if the two fields  $\psi$  and  $\phi$  are related by a simple time derivative and hence in quadrature. This is the case for the rotating Boussinesq equations as well as for the rotating shallow-water equations and therefore holds quite generally for gravity waves.

5.2. *Energy equipartition statement (2.36) for plane inertia–gravity waves*

We derive

$$(2.36) : \quad \hat{C}_W^b(k) + \left[ D_W^\psi(k) - k \frac{d}{dk} D_W^\psi(k) \right] = \left[ D_W^\phi(k) - k \frac{d}{dk} D_W^\phi(k) \right]$$

for a spectrum of stationary, homogeneous, horizontally isotropic, and hydrostatic plane inertia–gravity waves. We delay making the hydrostatic assumption until the end, so we start by assuming that the wavenumber vector  $(k, l, m)$  and the intrinsic frequency  $\omega$  are related by the full dispersion relation of the Boussinesq system with constant  $f$  and  $N$ :

$$(k_h^2 + m^2)\omega^2 = m^2 f^2 + k_h^2 N^2. \tag{5.5}$$

Next we derive the following equipartition statement for three-dimensional spectra:

$$\hat{C}_W^b(k, l, m) + k_h^2 \hat{C}_W^\psi(k, l, m) = k_h^2 \hat{C}_W^\phi(k, l, m) + \hat{C}_W^w(k, l, m). \tag{5.6}$$

For a plane wave with frequency  $\omega$  the linear buoyancy equation  $b_t + N^2 w = 0$  and the continuity equation  $w_z = -(u_x + v_y)$  imply

$$\omega^2 \hat{C}_W^b = N^2 \hat{C}_W^w \quad \text{and} \quad m^2 \hat{C}_W^w = k_h^4 \hat{C}_W^\phi. \tag{5.7}$$

Combining (5.7) with  $\omega^2 \hat{C}_W^\psi = f^2 \hat{C}_W^\phi$  from (2.33) and substituting in (5.6) yields

$$\left(1 - \frac{\omega^2}{N^2} + \frac{m^2}{k_h^2} \frac{f^2 - \omega^2}{N^2}\right) \hat{C}_W^b(k, l, m) = 0. \quad (5.8)$$

This holds by (5.5) and therefore establishes (5.6). The sought-after (2.36) then follows after integrating over  $l$  and  $m$  and dropping the  $\hat{C}_W^w$  term because of the hydrostatic approximation. Conversely, the non-hydrostatic version of (2.36) would be

$$\hat{C}_W^b(k) + \left[ D_W^\psi(k) - k \frac{d}{dk} D_W^\psi(k) \right] = \left[ D_W^\phi(k) - k \frac{d}{dk} D_W^\phi(k) \right] + \hat{C}_W^w(k). \quad (5.9)$$

This calculation does depend on the assumption of plane waves, e.g., if standing vertical modes were considered instead then the result would not hold, because the wave spectrum is then not homogeneous in the vertical. Mathematically, this is because the second equation in (5.7) does not hold for standing waves. Physically, this occurs because at nodal horizontal planes, where  $b = w = 0$  at all times, there is no potential energy at all and equipartition fails even for non-rotating waves.

#### REFERENCES

- BATCHELOR, G. K. 1953 *The Theory of Homogeneous Turbulence*. London: Cambridge University Press.
- CALLIES, JÖRN & FERRARI, RAFFAELE 2013 Interpreting energy and tracer spectra of upper-ocean turbulence in the submesoscale range (1-200 km). *Journal of Physical Oceanography* **43** (11), 2456–2474.
- CHARNEY, JULE G. 1971 Geostrophic Turbulence. *Journal of the Atmospheric Sciences* **28** (6), 1087–1095.
- FERRARI, RAFFAELE & RUDNICK, DANIEL L. 2000 Thermohaline variability in the upper ocean. *Journal of Geophysical Research* **105** (C7), 16857–16883.
- FERRARI, RAFFAELE & WUNSCH, CARL 2010 The distribution of eddy kinetic and potential energies in the global ocean. *Tellus A* **62** (2), 92–108.
- LINDBORG, ERIK 1999 Can the atmospheric kinetic energy spectrum be explained by two-dimensional turbulence? *Journal of Fluid Mechanics* **388**, 259–288.
- LINDBORG, ERIK 2007 Horizontal wavenumber spectra of vertical vorticity and horizontal divergence in the upper troposphere and lower stratosphere. *Journal of the atmospheric sciences* **64** (3).
- MÜLLER, PETER, LIEN, REN-CHIEH & WILLIAMS, ROBIN 1988 Estimates of potential vorticity at small scales in the ocean. *Journal of physical oceanography* **18** (3), 401–416.
- MUNK, WALTER H. 1981 Internal Waves and Small-Scale Processes. In *Evolution of Physical Oceanography* (ed. Bruce A. Warren & Carl Wunsch), chap. 9, pp. 264–291. Cambridge: The MIT Press.
- NASTROM, G. D. & GAGE, K. S. 1985 A Climatology of Atmospheric Wavenumber Spectra of Wind and Temperature Observed by Commercial Aircraft. *Journal of the Atmospheric Sciences* **42** (9), 950–960.
- RILEY, JAMES J & LINDBORG, ERIK 2008 Stratified turbulence: A possible interpretation of some geophysical turbulence measurements. *Journal of the Atmospheric Sciences* **65** (7).
- SMITH, LESLIE M & WALEFFE, FABIAN 2002 Generation of slow large scales in forced rotating stratified turbulence. *Journal of Fluid Mechanics* **451**, 145–168.
- TULLOCH, ROSS & SMITH, K. SHAFER 2006 A theory for the atmospheric energy spectrum: depth-limited temperature anomalies at the tropopause. *Proceedings of the National Academy of Sciences of the United States of America* **103** (40), 14690–14694.
- WAITE, MICHAEL L & BARTELLO, PETER 2004 Stratified turbulence dominated by vortical motion. *Journal of Fluid Mechanics* **517**, 281–308.
- WANG, DONG-PING, FLAGG, CHARLES N., DONOHUE, KATHLEEN & ROSSBY, H. THOMAS 2010 Wavenumber Spectrum in the Gulf Stream from Shipboard ADCP Observations and



Comparison with Altimetry Measurements. *Journal of Physical Oceanography* **40** (4), 840–844.

WORTHAM, CIMMARON, CALLIES, JÖRN & SCHARFFENBERG, MARTIN 2014 Asymmetries between wavenumber spectra of along- and across-track velocity from tandem-mission altimetry. *Journal of Physical Oceanography* **44** (4), 1151–1160.

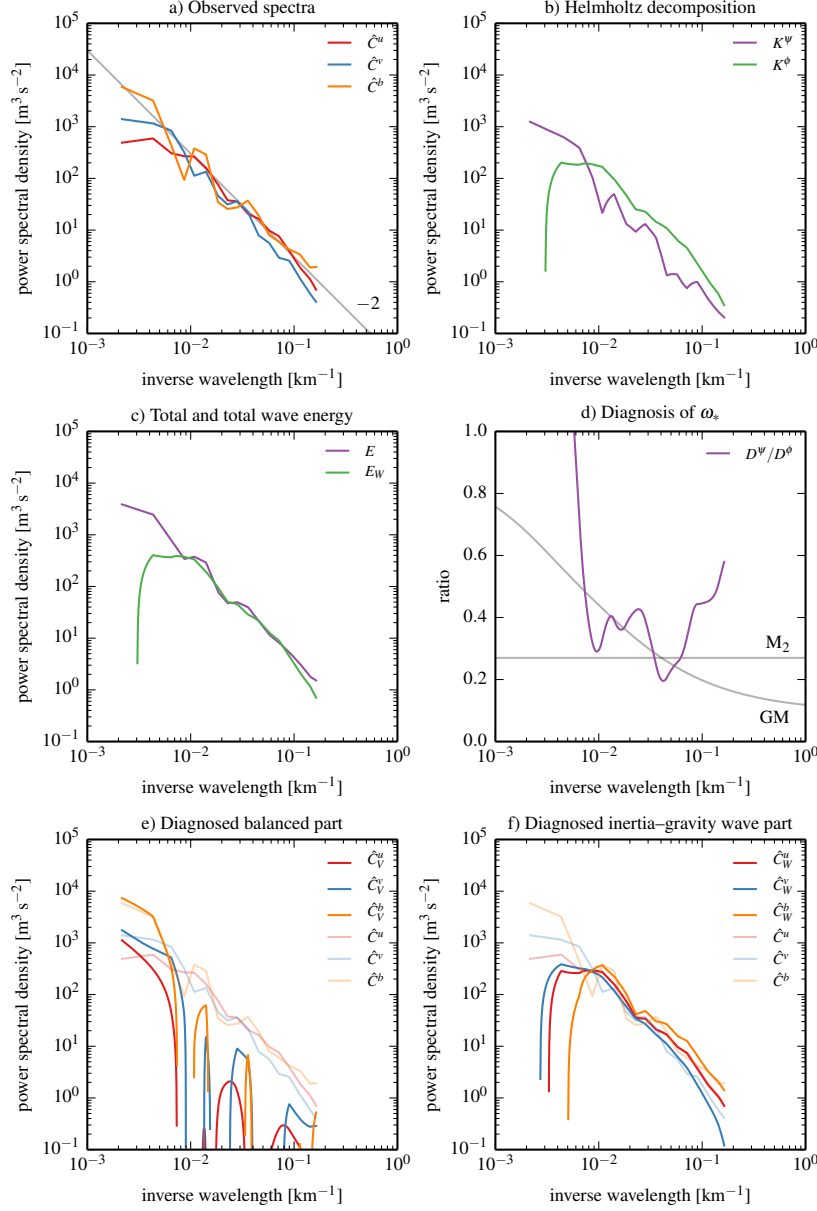


FIGURE 1. Observations from the eastern subtropical North Pacific: (a) observed transverse and longitudinal kinetic energy and potential energy spectra  $\hat{C}^u$ ,  $\hat{C}^v$ , and  $\hat{C}^b$ , (b) decomposition into rotational and divergent components  $D^\psi$  and  $D^\phi$  from (2.30–2.31) and (2.27); here  $K^\psi = \frac{1}{2}(D^\psi - kdD^\psi/dk)$  and  $K^\phi = \frac{1}{2}(D^\phi - kdD^\phi/dk)$ , (c) total observed energy  $E$  and total inertia–gravity wave energy  $E_W$  from (2.37), (d) ratio  $D^\psi/D^\phi$  compared to  $\omega_*$  from Garrett–Munk (GM) spectrum and  $M_2$  value for reference, (e) diagnosis of the balanced components of the observed spectra  $\hat{C}_V^u$ ,  $\hat{C}_V^v$ , and  $\hat{C}_V^b$ , (f) diagnosis of the inertia–gravity wave component of the observed spectra  $\hat{C}_W^u$ ,  $\hat{C}_W^v$ , and  $\hat{C}_W^b$ . In panel (a) a line corresponding to a  $k^{-2}$  power law has also been added for reference.

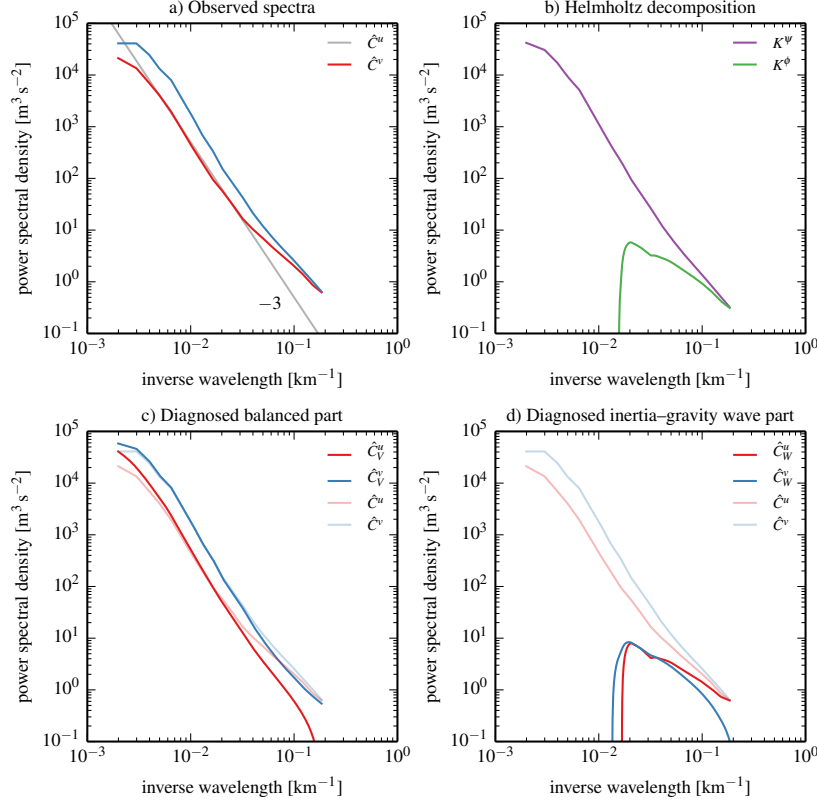


FIGURE 2. Observations from the Gulf Stream region: (a) observed transverse and longitudinal kinetic energy spectra  $\hat{C}^u$  and  $\hat{C}^v$ , (b) decomposition into rotational and divergent components  $D^\psi$  and  $D^\phi$  from (2.30–2.31) and (2.27); here  $K^\psi = \frac{1}{2}(D^\psi - kdD^\psi/dk)$  and  $K^\phi = \frac{1}{2}(D^\phi - kdD^\phi/dk)$ , (c) diagnosis of the balanced components of the observed spectra  $\hat{C}^u_V$  and  $\hat{C}^v_V$ , (d) diagnosis of the inertia–gravity wave component of the observed spectra  $\hat{C}^u_W$  and  $\hat{C}^v_W$ . In panel (a) a line corresponding a  $k^{-3}$  power law has also been added for reference.